Computational Examination of Orientation-Dependent Morphological Evolution during the Electrodeposition and Electrodissolution of Magnesium

S. DeWitt,[a,b,*] N. Hahn,[c] K. Zavadil,[c,] and K. Thornton[a,b,d,**,z]**

[a]*Joint Center for Energy Storage Research, University of Michigan, Ann Arbor, Michigan 48109, USA*
[b]*Applied Physics Program, University of Michigan, Ann Arbor, Michigan 48109, USA*
[c]*Joint Center for Energy Storage Research, Sandia National Laboratories, Albuquerque, New Mexico 87185, USA*
[d]*Department of Materials Science and Engineering, University of Michigan, Ann Arbor, Michigan 48109, USA*

A new model of electrodeposition and electrodissolution is developed and applied to the evolution of Mg deposits during anode cycling. The model captures Butler-Volmer kinetics, facet evolution, the spatially varying potential in the electrolyte, and the time-dependent electrolyte concentration. The model utilizes a diffuse interface approach, employing the phase field and smoothed boundary methods. Scanning electron microscope (SEM) images of magnesium deposited on a gold substrate show the formation of faceted deposits, often in the form of hexagonal prisms. Orientation-dependent reaction rate coefficients were parameterized using the experimental SEM images. Three-dimensional simulations of the growth of magnesium deposits yield deposit morphologies consistent with the experimental results. The simulations predict that the deposits become narrower and taller as the current density increases due to the depletion of the electrolyte concentration near the sides of the deposits. Increasing the distance between the deposits leads to increased depletion of the electrolyte surrounding the deposit. Two models relating the orientation-dependence of the deposition and dissolution reactions are presented. The morphology of the Mg deposit after one deposition-dissolution cycle is significantly different between the two orientation-dependence models, providing testable predictions that suggest the underlying physical mechanisms governing morphology evolution during deposition and dissolution.

Manuscript submitted September 29, 2015; revised manuscript received November 17, 2015. Published December 30, 2015. This was Paper 328 presented at the Chicago, Illinois, Meeting of the Society, May 24-28, 2015.

Magnesium batteries have garnered substantial attention as a successor to Li-ion batteries due to their potential for high energy density and safe operation.[1–3] Metallic Mg anodes provide a substantially higher specific volumetric capacity (3833 mA h/cm^3) than either Li-graphite anodes (760 mA h/cm^3) or metallic Li anodes (2046 mA h/cm^3).[2] Furthermore, unlike metallic Li anodes,[5] metallic Mg anodes can be cycled without the formation of dendrites.[4] Dendrite growth poses a hazard because dendrites can grow across the separator to the cathode and short the battery, leading to thermal runaway.[5,6] Instead of forming dendrites, metallic Mg anodes form compact, faceted films, practically eliminating this risk.[4] Understanding the evolution of this Mg film during cycling is a critical factor in the development of high-performance magnesium batteries.[7]

Although the development of electrolytes for the efficient and reversible deposition and dissolution of Mg has been pursued extensively (see Refs. 1 and 2 for comprehensive reviews on this topic), much less attention has been given to the morphological evolution of the Mg deposits during cycling. SEM and AFM images of the Mg film typically show a highly faceted film with grains on the order of 1 μm in width.[8–11] However, other morphologies with either larger[10] or smaller[12,13] features have also been observed.

The most comprehensive examination of the morphology of electrodeposited Mg was conducted by Matsui,[4] who examined the morphology of 1 C/cm^2 of Mg deposited at 0.5, 1, and 2 mA/cm^2. At 0.5 and 1 mA/cm^2, he observed very similar morphologies: round faceted grains 2-3 μm in diameter. In contrast, at 2 mA/cm^2, he observed a different morphology: triangular grains with sizes 0.5-1 μm. This transition in the morphology coincides with a change in preferred orientation from (0001) at 0.5 and 1 mA/cm^2 to (1010) at 2 mA/cm^2, determined from X-ray diffraction. Matsui also examined the film morphology for a smaller amount of deposited Mg (0.25 C/cm^2) and observed a large number of equally sized faceted spheres with a diameter of approximately 1.5 μm. Matsui hypothesized that Mg does not form dendrites because the electrolyte surrounding a newly formed nucleus is depleted to the point that nucleation at another point on the substrate is favored over deposit growth. Consequently, a high density of deposits forms on the surface prior to substantial growth. This even coverage of deposits prevents the current localization that leads to dendrite growth. Other mechanisms for the suppression of dendrites during Mg deposition have been suggested, including faster surface diffusion[2,14] and higher bond strength,[15] as compared to Li.

Simulations of Mg electrodeposition and electrodissolution may yield insight into mechanisms underlying these experimental observations of Mg film morphology and can provide a tool to predict anode morphology during cycling. Several models of electrodeposition can be found in the literature. Wheeler, Josell, and Moffat developed a two-dimensional (2D) model of copper electrodeposition using the level set method to track the moving interface.[16] This model accounts for the evolution of the concentration in the electrolyte, the reaction kinetics through the Butler-Volmer equation, and the effect of adsorbed accelerator species. Guyer et al. developed a one-dimensional (1D) phase field model for electrodeposition.[17,18] This model accounts for the concentration evolution in the electrolyte, the charge separation in the interfacial double layer, and the variation of the electric potential in the electrolyte. The thermodynamic underpinnings of this model provide a overpotential-current relationship consistent with Butler-Volmer kinetics. Ely, Jana, and Garcia[19] developed a 2D phase field model similar to the Guyer et al. model, but assumed a constant electrolyte concentration and explicitly used Butler-Volmer kinetics to model the reaction rate.

Many aspects of these models are applicable to Mg electrodeposition and electrodissolution, including Butler-Volmer reaction kinetics, electrolyte concentration evolution, and spatial variation of the potential in the electrolyte. However, unlike these previous models, evolution should be simulated in three dimensions (3D) to capture the 3D morphology of the deposits, which do not exhibit the rotational or translational symmetry that allows simplification to 1D or 2D. Furthermore, none of these models provide a framework for the formation and evolution of the facets observed experimentally.

*Electrochemical Society Student Member.
**Electrochemical Society Active Member.
[z]E-mail: kthorn@umich.edu

A formulation for modeling facet formation and evolution was developed for quantum dot growth via selective area epitaxy, taking a phase-field approach.[20,21] An orientation-dependent growth rate in the phase field equation leads to a faceted deposit morphology. The deposit morphology conforms to the shape predicted by the kinetic Wulff construction,[22] where the outwardly growing facets correspond to slow growth rate orientations and inwardly growing facets correspond to fast growth rate orientations. The model was implemented using the smoothed boundary method. The smoothed boundary method is a diffuse interface numerical method to restrict the solution of an equation to a particular subdomain within the computational domain and enforces boundary conditions along the boundary of the subdomain.[23] In Refs. 20 and 21, the smoothed boundary method is used to separate the vapor and deposit subdomains from the substrate subdomain.

The smoothed boundary method has also been used in combination with the standard dilute solution model of an electrolyte[24] to solve for the concentration evolution and potential distribution in the electrolyte for simulations of Li-ion battery cathodes.[25,26] There, the smoothed boundary method was used to restrict the equations governing the electrolyte and the electrode to their respective regions, as well as to apply boundary conditions between the two regions.

In this paper, we develop a new model of morphological evolution during electrodeposition and electrodissolution. This model combines the simulation approach for electrochemical processes with a static domain geometry from Ref. 25 and the diffuse interface model that describes the growth of faceted crystals from Ref. 20. Thus, the model is capable of describing the evolution of faceted magnesium deposits with growth rates and dissolution rates that vary in space and time according to the non-uniform potential and ionic concentrations in the electrolyte. Experimental observations were used to parameterize the model's orientation-dependent deposition rate, and the model is shown to reproduce the observed hexagonal plate deposit morphologies. Simulations predict that the deposit morphology changes as the applied current density increases as a result of the depletion of the electrolyte along the deposit surface. Simulations with varied spacing between nuclei provide support for Matsui's hypothesis[4] that electrolyte depletion can inhibit deposit growth and thereby promotes nucleation during the early stages of deposition. Predictions of the deposit morphology after one deposition-dissolution cycle are presented for two possible classes of phenomena that control the orientation dependence of the reaction rates. These predictions are used to propose an experiment to provide insight into the mechanisms responsible for the orientation-dependent growth and dissolution rates.

Model

Continuum model for the electrochemical evolution of faceted deposits.—In order to simulate the evolution of faceted Mg deposits, we have developed a new model of electrodeposition and electrodissolution. This model can be separated into three coupled models, each describing a different region of the system: the electrolyte-deposit interface, the electrolyte, and the Mg deposit. A schematic diagram of the system is given in Fig. 1.

The deposition/dissolution reaction occurs at the electrolyte-deposit interface. For simplicity, we assume that the dominant overall reaction is

$$Mg^{2+}(l) + 2e^{-}(s) \rightleftharpoons Mg(s) \quad [1]$$

If we assume that the first electron transfer during deposition is much faster than the second electron transfer during deposition,[2] the current associated with this reaction, i_{rxn}, can be given by a Butler-Volmer expression[24]

$$i_{rxn} = k_{dep} c_{ion}^{int} \exp\left(\frac{-\beta F(\phi_{we} - \phi_{int})}{RT}\right) - k_{dis} \exp\left(\frac{(2-\beta)F(\phi_{we} - \phi_{int})}{RT}\right) \quad [2]$$

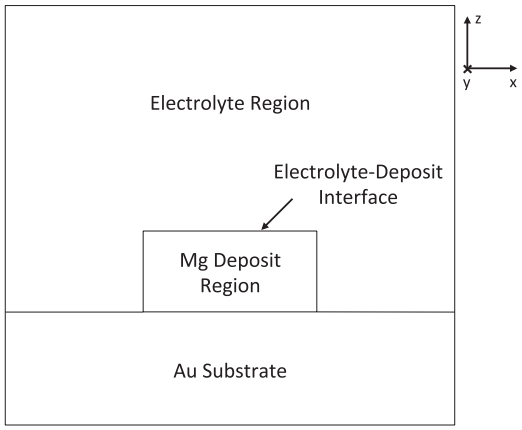

Figure 1. Schematic 2D diagram of the model system.

where F is Faraday's constant, k_{dep} is the rate constant for deposition, k_{dis} is the rate constant for dissolution, c_{ion}^{int} is the concentration of Mg^{2+} in the electrolyte at the electrolyte-deposit interface, β is the symmetry factor, R is the gas constant, and T is the temperature. The potential of the working electrode (the combination of the substrate and the deposit) is assumed to be spatially constant and is given by ϕ_{we}. The potential on the electrolyte side of the electrolyte-electrode interface is denoted by ϕ_{int}.

In general, k_{dep} and k_{dis} can depend on the local orientation of the Mg deposit. This orientation-dependence can take the form of

$$k_{dep} = k_{dep}^{*} \tilde{k}_{dep}(\theta_1, \theta_2) \quad [3]$$

$$k_{dis} = k_{dis}^{*} \tilde{k}_{dis}(\theta_1, \theta_2) \quad [4]$$

where k_{dep}^{*} and k_{dis}^{*} are rate coefficients set by the exchange current density and $\tilde{k}_{dep}$ and $\tilde{k}_{dis}$ are anisotropy functions that describe the orientation-dependence of the reaction rate. The local deposit orientation is described by two angles, θ_1 and θ_2: θ_1 is the angle between the deposit surface normal and the plane of the substrate, and θ_2 is the azimuthal angle, which is taken to be the angle between the x-axis and the projection of the deposit surface normal onto the plane of the substrate. The anisotropy functions can be further separated into the product of functions solely dependent on either θ_1 or θ_2: $\tilde{k}_{dep}(\theta_1, \theta_2) = \tilde{k}_{dep1}(\theta_1)\tilde{k}_{dep2}(\theta_2)$ and $\tilde{k}_{dis}(\theta_1, \theta_2) = \tilde{k}_{dis1}(\theta_1)\tilde{k}_{dis2}(\theta_2)$. The orientation-dependence of k_{dep} and k_{dis} can lead to the formation of facets on the deposit. Therefore, k_{dep} and k_{dis} are similar to the orientation-dependent growth velocity in Ref. 20, except that the growth velocity in this model also depends on the other variables in Eq. 2. Two possible models relating $\tilde{k}_{dep}$ and $\tilde{k}_{dis}$ will be discussed later in this section.

In the electrolyte, we calculate the distribution of the electric potential and the evolution of the concentration of the active species. Although the speciation of the electrolytes used for Mg deposition and dissolution is often quite complex,[1] in the interest of simplicity, we assume that the active species in the electrolyte are Mg^{2+} and A^{2-}, where A is a generic divalent anion. Applying the usual assumption of bulk electroneutrality,[24] the concentrations of these two species are equal throughout the electrolyte and given by c_{ion}. Following the typical derivation for a dilute binary electrolyte,[24] the evolution of the concentration is given by

$$\frac{\partial c_{ion}}{\partial t} = \nabla \cdot (D \nabla c_{ion}) \quad [5]$$

where $D = (z_{Mg} u_{Mg} D_A - z_A u_A D_{Mg})/(z_{Mg} u_{Mg} - z_A u_A)$, $z_{Mg} = 2$ is the valence of the Mg cation, $z_A = -2$ is the valence of A, u_{Mg} is the mobility of the Mg ions, u_A is the mobility of the A ions, D_{Mg} is the diffusivity of the Mg ions, and D_A is the diffusivity of the A ions. The mobilities of the Mg and A ions, u_{Mg} and u_A, can be expressed in terms of their diffusivity through the Nernst-Einstein relation:[24]

$u_{Mg} = D_{Mg}/RT$ and $u_A = D_A/RT$. Also from the typical treatment of a dilute binary electrolyte,[24] the distribution of the potential is given by a current continuity relation:

$$\nabla\cdot\mathbf{i} = -z_{Mg}F\nabla\cdot[(z_{Mg}u_{Mg} - z_A u_A)Fc_{ion}\nabla\phi + (D_{Mg} - D_A)\nabla c_{ion}] = 0 \quad [6]$$

Equations 5 and 6 are solved only within the electrolyte.

According to the reaction in Eq. 1, the flux of A^{2-} at the electrolyte-deposit interface is zero and the flux of Mg^{2+} at the electrolyte-deposit interface is equal to the reaction flux. The combination of these two flux expressions yield the following flux relation at the electrolyte-deposit interface:[25]

$$\mathbf{J}\cdot\mathbf{n} = -\frac{(1 - t_{Mg})i_{rxn}}{z_{Mg}F} \quad [7]$$

where $\mathbf{J}\cdot\mathbf{n}$ is the ionic flux at the electrolyte-deposit interface and $t_{Mg} = (z_{Mg}u_{Mg})/(z_{Mg}u_{Mg} - z_A u_A)$ is the Mg transference number.

The evolution of the Mg deposit is modeled using a phase field approach similar to that used to model InGaN quantum dot growth by selective area epitaxy.[20,21] As in many previous publications,[20,21,27–30] the phase field model is applied as a computational model to track the interfacial position, rather than as a physical model of phase transformation. The region occupied by the Mg deposit is described by a phase field parameter, $c_{deposit}$, where $c_{deposit} = 1$ within the deposit and $c_{deposit} = 0$ outside the deposit. Therefore, $c_{deposit}$ can be thought of as the normalized concentration of metallic Mg.

The evolution of $c_{deposit}$ is given by the Cahn-Hilliard equation[31] with a source term, $vBc_{deposit}^2(1 - c_{deposit})^2$, to account for deposition or dissolution:[20,21,27,28]

$$\frac{\partial c_{deposit}}{\partial t} = \nabla\cdot\left[M(c_{deposit})\nabla\left(\frac{\partial f}{\partial c_{deposit}} - \kappa^2\nabla^2 c_{deposit}\right)\right] + vBc_{deposit}^2(1 - c_{deposit})^2 \quad [8]$$

where $M(c_{deposit})$ is the mobility of Mg in the deposit, f is the bulk free energy density, κ is the gradient energy coefficient, which adds an energetic penalty for interfaces between the deposit and the electrolyte, v is the normal velocity of the interface, and B is a normalization factor. The Mg mobility along the surface of the deposit is expected to be much higher than the mobility through the bulk. Therefore, as in Ref. 20, we define $M(c_{deposit}) = M_s c_{deposit}^2(1 - c_{deposit})^2$, where M_s is the surface mobility of Mg. Sharp interface analysis demonstrates that this formulation of the mobility is equivalent to surface diffusion along the electrolyte/deposit interface in the sharp interface limit.[27]

Following the derivation in Ref. 20, the bulk free energy density is modeled by $f(c_{deposit}) = Wc_{deposit}^2(1 - c_{deposit})^2$. This free energy function has minima at $c_{deposit} = 0$ and $c_{deposit} = 1$ and an energetic barrier of height $W/16$ at $c_{deposit} = 0.5$. Thus, the free energy function promotes phase separation, with regions where $c_{deposit}$ is either 0 or 1. The gradient energy penalty term, $\kappa^2\nabla^2 c_{deposit}$, penalizes a sharp transition between these two regions, thus generating a thin interfacial region of finite thickness with intermediate values of $c_{deposit}$.

The normal velocity is determined by a combination of Eq. 2 and Faraday's law:

$$v = \frac{i_{rxn}\Omega_{Mg}}{z_{Mg}F} \quad [9]$$

where Ω_{Mg} is the molar volume of Mg. The normalization factor, $B = \sqrt{72W}/\kappa$, is determined from a sharp interface analysis.[27] The expression $c_{deposit}^2(1 - c_{deposit})^2$ is nonzero only near the interface and thus the source term is limited to the interface.

Equation 8 is solved only in the deposit and the electrolyte, and the substrate is assumed to be stationary throughout the process.

Two models of reaction rate orientation dependence.—The orientation-dependence of the reaction rate, as represented by $\tilde{k}_{dep}$ and $\tilde{k}_{dis}$ in our model, could be a result of orientation dependence in one of several properties for the electrolyte-deposit interface including: the kink-site density of the Mg surface, the existence and thickness of a passivation layer on the deposit, or the Mg ion's adsorption/desorption energy. These sources of orientation dependence may be symmetric (with respect to the reaction direction), i.e. $\tilde{k}_{dis} = \tilde{k}_{dep}$, or asymmetric, e.g. reciprocal where $\tilde{k}_{dis} = 1/\tilde{k}_{dep}$.

The kink-site density and the passivation layer thickness, $\tilde{k}_{dep}$ and $\tilde{k}_{dis}$ are expected to be symmetric sources because the reactivity of the Mg planes is due to properties of the planes that affect the reaction rate equally in both the deposition and dissolution reactions. If the orientation dependence is due to the adsorption/desorption energy, $\tilde{k}_{dep}$ and $\tilde{k}_{dis}$ can be represented as the exponential functions $\tilde{k}_{dep} = \exp(\Delta E_a/RT)$ and $\tilde{k}_{dis} = \exp(-\Delta E_a/RT)$, where ΔE_a is the adsorption energy. Thus, the anisotropy functions are expected to have a reciprocal relationship: $\tilde{k}_{dis} = 1/\tilde{k}_{dep}$. Both models have been examined in our simulations, and the effect of using a symmetric versus a reciprocal orientation dependence is discussed in the Results and discussion section.

Physical input parameters.—The physical parameters used in our model are given in Table I. The source of each of these parameters is briefly described below.

In Eq. 8, the barrier height coefficient and gradient penalty coefficient, W and κ respectively, were selected such that the equilibrium profile of $c_{deposit}$ has approximately four points in the interface. Both variables are normalized by a characteristic energy density, leaving W dimensionless and κ with units of nm. The value of $M_s = 6\times10^{-12}cm^2/s \times \frac{i_{app}}{1mA/cm^2}$ is selected such that there is sufficient diffusion for $c_{deposit}$ to maintain a smooth profile but not so much diffusion that the facets become rounded. The contact angle between the Mg deposit and the substrate, θ, is set to be 90°, based on top-down SEM images of Mg deposits (see the Experimental morphology subsection).

In Eq. 5, the diffusion constants for the electrolyte species, D_{Mg} and D_A, are set in accordance with the measurements in Ref. 33 that were conducted for a 0.4 M C_2H_5MgCl-$((C_2H_5)_2Al\ Cl)_2$/THF electrolyte. For consistency with this experimental system, c_{ion}^{bulk} is set to 0.4 M.

In Eq. 2, we make the common assumption that the change in energy barriers for the deposition and dissolution reactions are equally affected by the applied potential, and therefore we take $\beta = 0.5$.[24] The values for k_{dep}^* and k_{dis}^* are estimated using the isotropic exchange current density, i_0, and the relationship between k_{dep}^* and k_{dis}^* at 0V vs. a magnesium reference electrode. To relate the experimental value of the exchange current density, 1 mA/cm^2,[32] to k_{dep}^* and k_{dis}^*, we define the isotropic exchange current density, $i_0 = (k_{dep}^*)^{\beta}(k_{dis}^*)^{(1-\beta)}(c_{ion}^{bulk})^{\beta}$, where we assume the electrolyte is in the well-stirred limit ($c_{ion}^{int} = c_{ion}^{bulk}$). To complete the parameterization of k_{dep}^* and k_{dis}^*, we note that current is approximately zero at 0 V[10,33], and thus $k_{dis}^* \approx k_{dep}^* c_{ion}^{bulk}$ from Eq. 2. We assume $T = 300$K and that the molar volume of Mg, Ω_{Mg} in Eq. 9, is 14 cm^3/mol.[34]

Table I. Model Parameters.

Model Parameter:	Value:	
W	1	
κ	1 nm	
M_s	6×10^{-12} cm^2/s $\times \frac{i_{app}}{1mA/cm^2}$	
θ	90°	
D_{Mg}	3×10^{-9} cm^2/s	Ref. 33
D_A	3×10^{-9} cm^2/s	Ref. 33
c_{ion}^{bulk}	0.4 M	
β	0.5	
k_f^*	2.5 mA/cm$^2\cdot M$	
k_b^*	1 mA/cm^2	
T	300 K	
Ω_{Mg}	14 cm^3/mol	Ref. 34

Computational Methods and Numerical Parameters

The governing equations, Eqs. 2, 5, 6 and 8, are solved in a computational domain containing regions that evolve in time. In Ref. 20, the boundary condition between the growing quantum dot and the immobile substrate was applied using the smoothed boundary method (SBM). The SBM is designed to restrict the solution of an equation to a subdomain within the larger computational domain and to efficiently apply boundary conditions along the boundary of that subdomain.[23] Like phase-field methods, the SBM is a diffuse interface method where a domain parameter defines the location of the subdomain and smoothly transitions between a value of 1 inside the subdomain and a value of 0 outside the subdomain.

Written in SBM form, Eq. 8 becomes[20,23]

$$\frac{\partial c_{deposit}}{\partial t} = \frac{1}{\psi}\nabla\cdot\left[\psi M(c_{deposit})\nabla\left(\frac{\partial f}{\partial c_{deposit}} - \frac{\kappa^2}{\psi}\left(\nabla\cdot\psi\nabla c_{deposit} + \frac{|\nabla\psi|\sqrt{2f}}{\kappa}\cos\theta\right)\right)\right] + vBc_{deposit}^2(1-c_{deposit})^2 \quad [10]$$

where ψ is a domain parameter with $\psi = 1$ in the electrolyte and Mg deposit and $\psi = 0$ in the substrate. The SBM is used to ensure that Eq. 8 is solved only in the electrolyte and Mg deposit.

Periodic boundary conditions are applied on the surfaces of the computational domain perpendicular to the surface of the substrate for Eq. 10. A no-flux boundary condition is applied at the top surface of the computational domain (the boundary between the computational domain and the bulk electrolyte). As in Ref. 20, the SBM is used to enforce a no-flux boundary condition along the substrate interface and to enforce a contact angle boundary condition, θ, at the triple phase boundary between the electrolyte, the deposit, and the substrate. The contact angle is determined by the balance of interfacial tensions between the three phases.[35]

As in Ref. 20, a curvature cutoff, H_c, is applied to prevent excess deposition/dissolution at the intersections between facets. These intersections are rounded, an artifact of the diffuse interface approach, leading to rate constants much higher than on the facets. The curvature, H, is given by the divergence of the interfacial normal vector of the Mg deposit:

$$H = \nabla\cdot\mathbf{n} = \nabla\cdot\left(\frac{\nabla c_{deposit}}{|\nabla c_{deposit}|}\right) \quad [11]$$

Based on this definition of the curvature, concave portions of the Mg deposit surface have positive curvature. During deposition, the rate constants k_{dep} and k_{dis} are set to zero in areas of high convex curvature, where the curvature is negative and greater in magnitude than H_c. Conversely, during dissolution deposition, k_{dep} and k_{dis} are set to zero in areas of high concave curvature, where the curvature is greater than H_c.

The SBM is also used to solve Eq. 5 and 6 only in the electrolyte. The SBM forms of these equations were obtained from Ref. 25:

$$\frac{\partial c}{\partial t} = \frac{1}{\psi_l}\nabla\cdot(\psi_l D\nabla c) - \frac{|\nabla\psi_l|}{\psi_l}\frac{i_{rxn}(1-t_{Mg})}{z_{Mg}F} \quad [12]$$

$$\nabla\cdot\left[\psi_l(z_{Mg}u_{Mg} - z_A u_A)Fc\nabla\phi\right] + |\nabla\psi_l|\frac{i_{rxn}}{z_{Mg}F} = \nabla\cdot\left[\psi_l(D_A - D_{Mg})\nabla c\right] \quad [13]$$

The domain parameter for the electrolyte, ψ_l, can be found by the simple relation $\psi_l = \psi(1 - c_{deposit})$.

To prevent current from erroneously flowing through the substrate-electrolyte interface near the substrate-electrolyte-deposit triple phase boundary, the boundary given by ψ_l must be decomposed into two regions: the substrate-electrolyte interface and the deposit-electrolyte interface. The expression localizing the boundary condition in Eqs. 15 and 16, $|\nabla\psi_l|$, can thus be separated into $|\psi\nabla(1-c_{deposit})| + |(1-c_{deposit})\nabla\psi|$. Along the substrate-electrolyte interface, i_{rxn} is assumed to be zero and therefore the second term can be dropped, leaving the boundary terms proportional to $|\psi\nabla(1-c_{deposit})|i_{rxn}$:

$$\frac{\partial c}{\partial t} = \frac{1}{\psi_l}\nabla\cdot(\psi_l D\nabla c) - \frac{|\psi\nabla(1-c_{deposit})|}{\psi_l}\frac{i_{rxn}(1-t_{Mg})}{z_{Mg}F} \quad [14]$$

$$\nabla\cdot\left[\psi_l(z_{Mg}u_{Mg} - z_A u_A)Fc\nabla\phi\right] + |\psi\nabla(1-c_{deposit})|\frac{i_{rxn}}{z_{Mg}F} = \nabla\cdot\left[\psi_l(D_A - D_{Mg})\nabla c\right] \quad [15]$$

Periodic boundary conditions are applied on the surfaces of the computational domain perpendicular to the surface of the substrate for both Eqs. 14 and 15. The top surface of the domain is taken to be the reference for the potential and is set to 0 V. To simulate galvanostatic processes with an applied current, i_{app}, we systematically select ϕ_{we} using a bisection scheme until the total reaction current is within $\delta_i \cdot i_{app}$ of i_{app}, where δ_i is the convergence tolerance. The boundary condition for ϕ in Eq. 6 along the electrolyte-electrode interface is $\phi = \phi_{int}$, where ϕ_{int} is calculated such that $i_{rxn} = \mathbf{i}\cdot\mathbf{n}$ at the electrolyte-electrode interface. The value of c_{ion} at the top surface of the computational domain is fixed at the bulk electrolyte value, c_{ion}^{bulk}.

The SBM formulations of the governing equations are solved using a finite difference scheme. Equation 10 is discretized using the semi-implicit Crank-Nicolson scheme and is solved using the Gauss-Seidel method with red-black ordering. Equation 14 is spatially discretized using second-order central finite differencing and is temporally discretized using the backward (implicit) Euler method. The resulting matrix equation is solved using successive overrelaxation (SOR) with Chebyshev acceleration.[36] Equation 15 is discretized using second-order central finite differencing, and, like Eq. 14, is solved using SOR with Chebyshev acceleration.

The computational expense of solving the model equations can be substantially reduced by replacing the full 3D equations governing the electrolyte with their corresponding 1D approximations away from the surface of the working electrode. The computational domain must extend far enough in the z direction such that the concentration at the far edge of the cell does not deviate from the bulk value. To accomplish this, the domain must be larger than the diffusion length (approximately 1,000 nm for a 1 s simulation). For most of this domain, the variation of c_{ion} and ϕ in the x-y plane is expected to be negligible and the electrolyte can be modeled as a 1D system. The full 3D treatment is necessary only within a few tens of nanometers of the substrate. Therefore, we split the computational domain into two parts. Within a distance L_{3D} of the working electrode, we solve the full 3D equations as given by Eqs. 10,14 and 15. For the remaining part of the computational domain with length L_{1D}, we solve the 1D analogs of Eqs. 6 and 7. Both of these 1D equations are solved implicitly using the tridiagonal matrix algorithm. The values of c_{ion} and ϕ on the substrate side of the 1D domain are used as boundary conditions for the top of the 3D domain. Solving the 1D analog of Eq. 10 is unnecessary because $c_{deposit}$ is uniformly zero in the 1D domain.

Each of $\tilde{k}_{dep1}(\theta_1)$, $\tilde{k}_{dep2}(\theta_2)$, $\tilde{k}_{dis1}(\theta_1)$, and $\tilde{k}_{dis2}(\theta_2)$ is tabulated in a lookup table with an interval of 1°. The values of $\tilde{k}_{dep}(\theta_1,\theta_2)$ and $\tilde{k}_{dis}(\theta_1,\theta_2)$ are determined by a linear interpolation between the tabulated values. To prevent small errors in the calculation of the orientation of a facet from causing a drastic change in the anisotropy functions, the value within ±2° of each facet orientation is set to the value at the tip of the cusp.

The finite difference calculations were parallelized using Message Passing Interface (MPI). A typical simulation took two hours using 128 2.67 GHz computing cores.

The numerical parameters for our simulations are given in Tables II and III. Unless otherwise stated, the 3D domain is 100 nm × 100 nm × 75 nm and is discretized into an even grid of 128 points × 128 points × 96 points. The length of the 1D domain, L_{1D}, is 9,000 nm and is discretized into $N_{1D} = 500$ points with linearly increasing grid spacing. The i^{th} point of the 1D grid is

Table II. Numerical parameters for the simulations

Numerical Parameter:	Value:
Grid points (3D)	128 × 128 × 96
Domain Size (3D)	100 nm × 100 nm × 75 nm
Grid points (1D)	500
Domain Size (1D)	9000 nm
r_{init}	10 nm
H_c	-0.13 nm^{-1}, 0.03 nm^{-1}
$\delta c_{deposit}$	1e-6
R_c	4e-7 M/s
R_ϕ	9e-2 M/s
$\delta\phi_{rxn}$	1e-7 V
δ_i	0.01

given by

$$z_{1D}(i) = \frac{(L_{1D} - N_{1D}\Delta z_{3D})}{N_{1D}^2} i^2 + \Delta z_{3D} i + L_{3D} \quad [16]$$

where Δz_{3D} is the grid spacing in the 3D domain.

At the beginning of each simulation, the electrolyte concentration is uniformly equal to the bulk value. During deposition H_c was set to -0.13 nm^{-1}, and during dissolution it was set to 0.03 nm^{-1}. These cutoffs were chosen such that the misorientation of the facets is generally less than 3° and the artificial rounding of the facet corners is limited. Each simulation has a uniform time step, which depends on the applied current. The time steps are scaled such that the amount of charge passed per time step is the same for different applied currents, and are given in Table III.

The tolerances for the convergence of the model equations were selected such that tighter tolerances have a minimal effect on the solution. The iterative solution for Eq. 10 is considered to have converged when the difference between successive values of $c_{deposit}$ is less than $\delta c_{deposit}$. The iterative solution for Eq. 14 is considered to have converged when the residual of Eq. 14 is less than R_c. Solving for ϕ occurs in two stages. First, Eq. 15 is solved using the SOR method with i_{rxn} linearized around ϕ_{int}. The iterative solution for Eq. 15 is considered to have converged when the residual of Eq. 14 is less than R_ϕ. Based on the resulting ϕ, an updated approximation of i_{rxn} is then calculated. This process continues until the difference in ϕ between successive iterations is less than $\delta\phi_{rxn}$, thus enforcing the full nonlinear expression of i_{rxn}. As described earlier, ϕ_{we} is found using a bisection method such that the current is within $\delta_i \cdot i_{app}$ of i_{app}.

In the simulations, two geometries were used for the initial Mg deposit. Most of the simulations were initialized using a hemispherical initial deposit with radius $r_{init} = 10$ nm. This initial deposit morphology is used for simulations where the basal plane of the Mg crystal structure is assumed to be parallel to the substrate, leading to short, broad deposits (termed in-plane deposits in the Experimental morphology subsection). However, in two of the simulations, the basal plane is assumed to be perpendicular to the substrate, leading to tall, narrow deposits (termed out-of-plane deposits in the Experimental morphology subsection). For one of these simulations, a 10-nm radius hemisphere was used as the initial condition. For the other simulation, an alternative initial geometry was used: an oblate hemispheroid extending 20 nm in the x direction, 10 nm in the y direction, and 10 nm in the z direction. This alternative geometry was chosen such that the maximum ratio of the thickness of the deposit parallel to the basal plane to the thickness of the deposit perpendicular to the basal plane is 2:1, just as it is for the hemispherical deposits when the basal plane is parallel to the substrate. As discussed later in the Results section, the simulated morphology resulting from the oblate hemispheroidal initial condition was closer to the kinetic Wulff shape than the morphology resulting from the hemispherical initial condition, because it reduced the effect of the finite size of the initial deposit on the simulated deposit morphology. The two initial deposit geometries can be seen in Fig. S1.

Table III. Time step for various applied current values.

i_{app} (mA/cm^2):	Δt (s):
1.5	8.33×10^{-4}
5	2.50×10^{-4}
10	1.25×10^{-4}

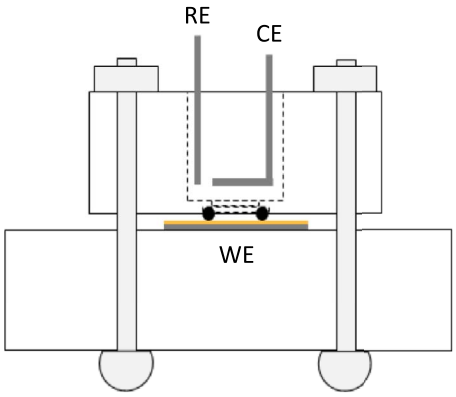

Figure 2. Basic schematic of the custom-built electrochemical cell used to perform Mg deposition onto planar Au/Si substrates. WE = working electrode, RE = reference electrode, CE = counter electrode. The O-ring was composed of an ether-resistant perfluoroelastomer (Kalrez).

Experimental

Electrolyte syntheses and electrochemical experiments were performed in an argon-filled glove box with background water levels below 0.2 ppm. The "all-phenyl-complex" (APC) electrolyte[37] was used for simplicity and was synthesized from solutions of PhMgCl (2 M solution in THF, Sigma-Aldrich) and $AlCl_3$ (99.99%, anhydrous, Sigma-Aldrich) in ultra-dry THF (J.T. Baker) and contained a total Mg concentration of 0.4 M. Initial water measurements made for the THF solvent were below 10 ppm, and water measurements for the final electrolyte composition were not attainable due presence of organometallic species (e.g., PhMgCl, $AlPh_xCl_{4-x}^-$, and Ph^2Mg), which interfere with accurate Karl-Fischer titration. Due to their chemically reducing nature, these organometallic species are also expected to react with any residual water molecules, yielding a nominally water-free electrolyte. We assume similar bulk speciation and transport properties for the active ions in the APC electrolyte and the dichloro-complex (DCC) electrolyte that was used to determine the model parameters. The Mg depositions were performed on highly textured Au (111) thin films deposited on silicon wafers. These Au/Si substrates were successively cleaned in acetone and piranha solution (3:1 H_2SO_4:H_2O_2) followed by extensive rinsing with deionized water and blow-drying under nitrogen. Electrochemistry was performed in a custom-made Kel-F cell, shown schematically in Fig. 2, using Mg ribbon (99.5%, Aldrich) counter and reference electrodes. Mg was deposited under galvanostatic control at approximately 1.5 mA/cm^2 for times ranging from 3 to 60 seconds. In all cases consistent structural motifs were attained although slight differences in nucleation density were observed, likely correlating with subtle changes in electrode surface cleanliness. The samples were rinsed with THF following deposition and imaged on a FEI Magellan SEM using an accelerating voltage of 500 V.

Results and Discussion

Experimental morphology.—The morphology of Mg deposits grown at approximately 1.5 mA/cm^2 can be seen in Fig. 3. After 5 seconds of growth, many of the deposits have not yet merged and have a faceted plate morphology with a broad facet on top and

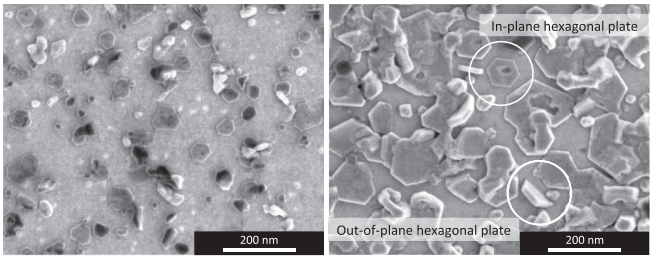

Figure 3. SEM images of Mg deposited on a (111) Au surface after (a) 5 seconds of deposition (b) 20 seconds of deposition at 1.5 mA/cm^2. Examples of in-plane and out-of-plane hexagonal plates are circled.

short faceted sides. The angles between most of the side facets are approximately 120°. The characteristic size for the deposits can be defined as the length of the shortest line through the center of the deposit crossing from one side of the deposit to another. Using this metric and sampling over a 500 nm × 500 nm area, the characteristic size after 5 seconds of growth ranges from approximately 10 to 60 nm. The maximum spacing between deposit centers is approximately 100 nm. After 20 seconds of growth, most of the deposits have merged, creating a less well-defined deposit morphology. However, the faceted surface and the 120° angles between side facets are still present. The characteristic size of the deposits is now ranges from approximately 10 to 160 nm. Two primary morphologies dominate at this stage: in-plane and out-of-plane hexagonal plates (with respect to the substrate surface). An example of each of these morphologies is circled in Fig. 3b. The out-of-plane hexagonal plates vary in their orientation from deposits with broad facets that are perpendicular to the substrate to deposits that are tilted by approximately 30° from the normal of the substrate.

Without cross-sectional images, the thicknesses of the in-plane plates cannot be directly measured. However, an estimate of the aspect ratio of these deposits can be obtained by measuring the ratio of the thicknesses of the long and short axes of a out-of-plane plate. The out-of-plane plate directly to the left of the circled in-plate plate in Fig. 3b has a long-to-short axis ratio of 5:1 (70 nm to 14 nm). Assuming both types of plates are the result of rotations from the same kinetic Wulff construction, the width-to-height ratio for the in-plane plates should be twice the long-to-short axis ratio for the out-of-plane plates because the deposits do not grow into the substrate. Therefore, the expected width-to-height ratio for the in-plane plates is 10:1.

Growth morphologies of individual deposits.—Using the aspect ratios for the hexagonal plates, we constructed anisotropy functions, $\tilde{k}_{dep}(\theta_1, \theta_2) = \tilde{k}_{dis}(\theta_1, \theta_2)$, assuming the symmetric orientation-dependence model. The components of $\tilde{k}_{dep}(\theta_1, \theta_2)$ are shown in Fig. 4. The expressions for these functions can be found in the Supplementary Material.

Figure 5 shows the simulated deposit morphology using these anisotropy functions with 0° and 90° rotations of the anisotropy about the x axis. The simulations were conducted at 1.5 mA/cm^2 for 5 s, as in the experimental results shown in Fig. 3a. We focus on the experimental morphologies at 5 s, because at 20 s most of the deposits have merged, obscuring the morphologies of the individual deposits. The simulated area of the electrode, 100 nm × 100 nm, was chosen to match the spacing between the simulated deposits to the maximum experimental spacing between deposits after 5 s so as to simulate the growth of well-separated deposits.

The in-plane hexagonal plate in Fig. 5 has width of 66 nm, growing 46 nm from the 20 nm diameter of the initial nucleus. This 46 nm of growth after 5 s of deposition is in agreement with the 10 to 60 nm deposit sizes observed in Fig. 3a.

The dependence of the morphology after 5 s of growth on the initial deposit morphology can be seen by comparing Fig. 5b with Fig. 5c. The simulations shown in Figs. 5b and 5c were initialized with the

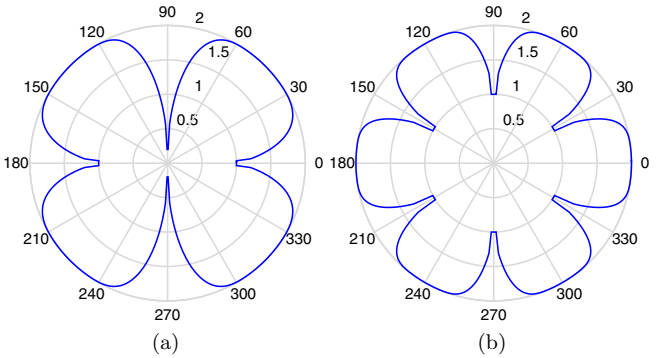

Figure 4. Polar plots of the components of $\tilde{k}_{dep}$ in the (a) θ_1 and (b) θ_2 directions during deposition. The cusps in these plots denote the location of the facets during growth. The product of these two functions yields the full anisotropy function.

hemispherical initial geometry (1:1 ratio of the widths in the x and y directions) and the oblate hemispheroidal initial geometry (2:1 ratio of the widths in the x and y direction) described in the Computational methods and numerical parameters section, respectively. The higher initial aspect ratio of the initial condition in Fig. 5c results in a deposit with a higher aspect ratio after 5 s of deposition, closer to the 5:1 ratio expected from the kinetic Wulff shape. In principle, the shape of the initial deposit should not change the predicted steady-state shape of the deposit. However, the dependence on the initial deposit shape persists due to the relatively large size of the initial deposit, as compared to the size of the deposit after 5 s of growth. As seen in Figs. 5b and 5c, the appropriate choice of the initial geometry can reduce artifacts due to the finite size of the initial deposit without having to significantly increase the spatial resolution of the simulation.

Effect of the applied current on the deposit morphology.—For simulations like those presented in the previous subsection that are performed at an applied current of 1.5 mA/cm^2, the electrolyte concentration at the electrode surface is effectively uniform, as can be seen in Fig. 6a. The electrolyte concentration is also effectively uniform at 5 mA/cm^2, as seen in Fig. 6b. However, as the current density increases to 10 mA/cm^2, the spatial variation in the electrolyte concentration along the electrode surface becomes noticeable, as seen in Fig. 6c. The concentration is particularly depleted at the sides of the deposit, where the reaction current on the faster-growing side facets has consumed more Mg^{2+} from the electrolyte than on the slower-growing top facet.

The cross-sections of the deposits grown at these three applied current densities can be seen in Fig. 7. As the applied current density increases and the concentration near the side facets decreases, more of the current passes through the top facet and the deposits become narrower and taller. At 10 mA/cm^2, the electrolyte concentration at the junction between the deposit and the substrate has almost reached zero, inhibiting further growth in this region. As a result, the sides become slanted inward.

To eliminate the possibility that the inhomogeneity of the electric potential in the electrolyte is responsible for the morphological

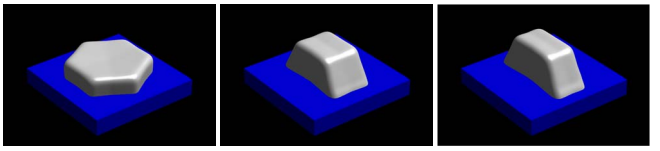

Figure 5. Simulated Mg deposits after 5 s of growth at 1.5 mA/cm^2. (a) An in-plane hexagonal plate deposit. (b) An out-of-plane hexagonal plate deposit where $\tilde{k}_{dep}(\theta_1, \theta_2)$ is rotated 90° about the x axis. (c) An out-of-plane hexagonal plate deposit using the oblate hemispheroidal initial geometry.

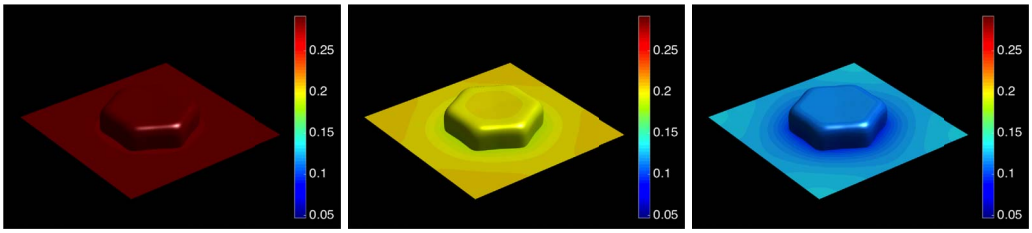

Figure 6. The electrolyte concentration at the electrode surface after 3 mC/cm^2 has passed at (a) 1.5, (b) 5, and (c) 10 mA/cm^2 with 100 nm spacing between deposits. The color represents the electrolyte concentration in mol/L.

change, rather than solely the concentration depletion observed above, we perform two additional simulations at 10 mA/cm^2. The inhomogeneity of the electric potential could plausibly cause the type of morphological change seen in Fig. 7 if the effects of the concentration gradient and the surface overpotential on the current distribution become negligible as the applied current density increases. Under these assumptions, which yield a potential termed the primary potential,[24] the potential is given by the Laplace equation with a Dirichlet boundary condition, and the current would be expected to be focused at the top of the deposit. Simulations assuming a well-stirred electrolyte, where the electrolyte concentration is uniform at a value equal to c_{ion}^{bulk}, and a well-supported electrolyte, where the potential drop across the bulk electrolyte is zero, are examined to separate the effects of the concentration and the potential in the electrolyte on the deposit morphology. The cross sections of the resulting deposits for these two simulations are shown in Fig. 8, along with the 10 mA/cm^2 cross section from Fig. 7. Under the unstirred/well-supported assumption, the deposit cross section is nearly identical to the unstirred/unsupported case. However, under the well-stirred/unsupported assumption, the deposit cross-section is more similar to the non-tapered deposits grown at a lower applied current. From these simulations, we can conclude that the morphology change is predominately due to the depletion of the electrolyte at the sides of the deposits.

Effect of the nucleus spacing on the electrolyte concentration.— Although the experimental image after 5 s of deposition (Fig. 3a) shows less than 100 nm spacing between deposits, earlier in the deposition process the spacing between neighboring deposits is larger because not all of the deposits have nucleated. To gain insight into this lower nuclei density regime, we performed three simulations similar to those in Fig. 6 but with 175 nm between the deposits (decreasing the density of the deposits by approximately a factor of three). The electrolyte concentration at the electrode surface for these simulations can be seen in Fig. 9. With larger spacing between the nuclei, variation in the electrolyte concentration near the deposit has increased at 10 mA/cm^2 and is now visible at 1.5 and 5 mA/cm^2. At 10 mA/cm^2, the electrolyte has depleted to approximately 10% of the bulk value. The minimum and maximum of the electrolyte concentration at the electrode surface for both the simulations with 100-nm and 175-nm spacing are given in Fig. 10a. The range between the minimum and maximum concentrations increases more than two-fold as the spacing increases from 100 nm to 175 nm, with the majority of the change due to the reduced minimum concentrations for 175 nm spacing.

As suggested by Matsui,[4] the depletion of the electrolyte near the deposit causes η to be higher near the deposit than it is away from the deposit, which would be expected to increase the likelihood of the nucleation of new deposits. This effect can be quantified by comparing the difference between the maximum and minimum of η along the working electrode, $\Delta\eta$. Figure 10b shows $\Delta\eta$ as a function of the applied current density and deposit spacing. As expected from the trends in the concentration data given in Fig. 10a, $\Delta\eta$ increases with increasing current density and with increasing deposit spacing. These simulations support Matsuis hypothesis that concentration depletion can cause nontrivial spatial variation in η.

Deposit cycling simulations.— In addition to simulating the growth of Mg deposits, our modeling approach enables simulations of deposition-dissolution cycles. The deposit morphology during dissolution depends on the model chosen for the orientation dependence of the reaction rate. Under the symmetric model described in the Model section, the components of $\tilde{k}_{dis}(\theta_1, \theta_2)$ are assumed to be equal to those for deposition, shown in Fig. 4. Using the standard facet selection criteria,[38] the dominant faces during dissolution are the fast-dissolving faces. Therefore, the dominant facets during dissolution are different than those during deposition and are located on the former edges of the hexagonal plate. Figure 11 shows the result of a simulation with 1.5 s of deposition followed by 1.2 s of dissolution, at a current density of $\pm$5 mA/cm^2. The deposit slowly transitions away

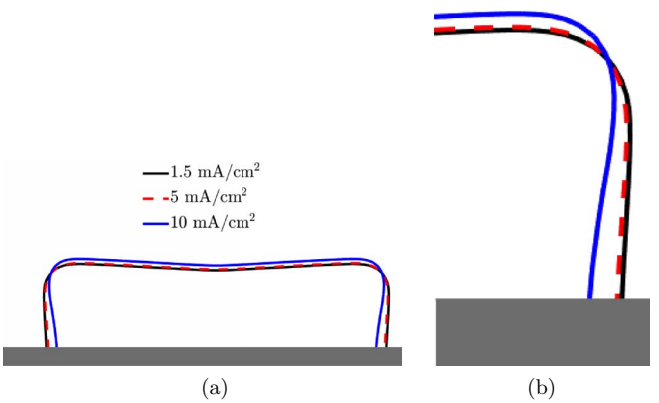

Figure 7. (a) The cross section of the Mg deposit (going through the side facets) after 6 mC/cm^2 has passed at 1.5, 5, and 10 mA/cm^2. (b) Magnified view of the cross section of the deposit edge.

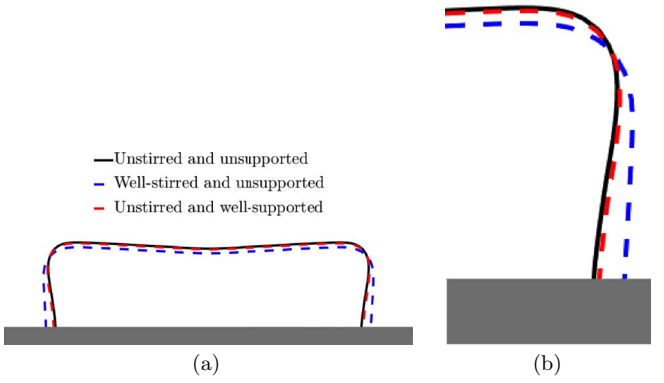

Figure 8. (a) The cross section of the Mg deposit for an unstirred/unsupported electrolyte, a well-stirred/unsupported electrolyte, and an unstirred/well-supported electrolyte after 6 mC/cm^2 has passed at 10 mA/cm^2. (b) Magnified view of the cross section of the deposit edge.

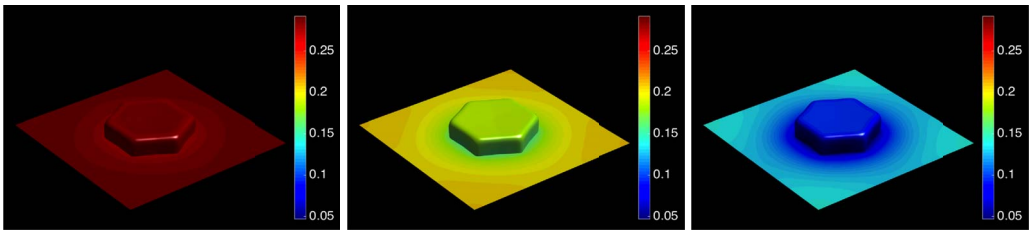

Figure 9. The electrolyte concentration at the electrode surface after 3 mC/cm^2 has passed at (a) 1.5, (b) 5, and (c) 10 mA/cm^2 with 175 nm spacing between deposits. The color represents the electrolyte concentration in mol/L.

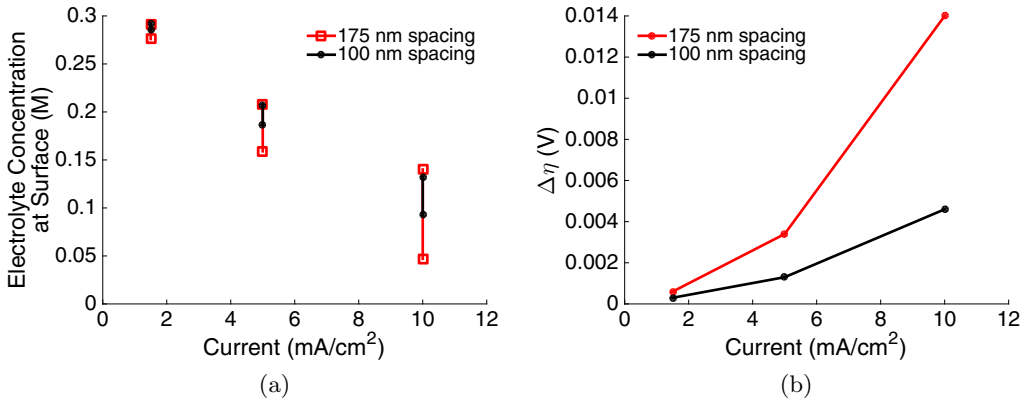

Figure 10. Plots of (a) the maximum and minimum of the electrolyte concentration along the electrode surface and (b) $\Delta\eta$, both after 3 mC/cm^2 has passed at 1.5, 5, and 10 mA/cm^2 for deposit spacings of 100 nm and 175 nm.

from the hexagonal plate morphology, with clearly defined 45° faces appearing after 1.0 s of dissolution. By the end of the simulation, the deposit has evolved into a flat-topped hexagonal pyramid.

In contrast, under the reciprocal model described in the Model section, the slowest growing planes are the fastest dissolving planes,

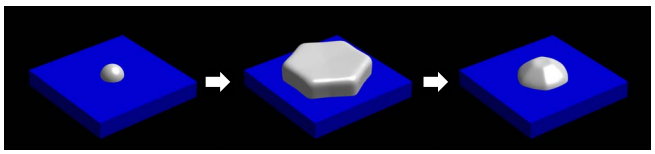

Figure 11. The evolution of the Mg deposit from an initial hemispherical nucleus (left), to its maximum size after 1.5 s of deposition (center), to its morphology following 1.2 s of dissolution, simulated using the symmetric model (right).

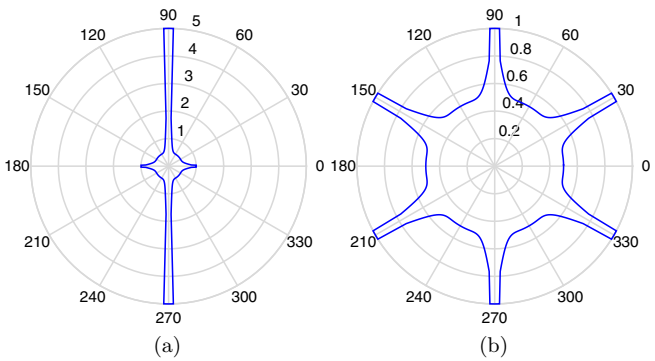

Figure 12. Polar plots of the components of $\tilde{k}_{dis}$ in the (a) θ_1 and (b) θ_2 directions during dissolution for the reciprocal model.

with the components of the anisotropy function for dissolution given in Fig. 12. Because the dominant faces during dissolution are the fast dissolving faces, the dominant faces under the reciprocal orientation-dependence model are the same during dissolution as they are during deposition. The morphology resulting from a simulation of a deposition-dissolution cycle using the reciprocal orientation-dependence model is shown in Fig. 13. As expected, the hexagonal plate morphology is maintained during dissolution. The lateral dimensions of the deposit are largely unchanged during dissolution, with nearly all of the volume change being due to a decrease in the height of the deposit. This observation is in stark contrast to what is observed during deposition, where most of the change is in the width of the deposit.

The predictions of the morphology of the hexagonal plate deposits during dissolution can be compared to the experimental morphology to determine whether the reaction is best described by the symmetric or reciprocal model. An experiment imaging the Mg deposits after partial dissolution would easily be able to discriminate between the hexagonal plate and hexagonal pyramid morphologies predicted by our simulations. The combination of this experiment and our model's continuum-scale predictions would yield insight into

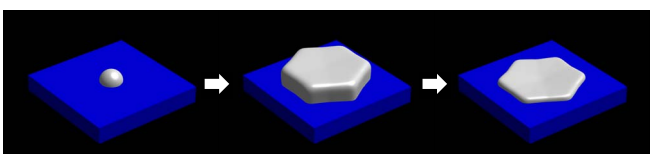

Figure 13. The evolution of the Mg deposit from an initial hemispherical nucleus (left), to its maximum size after 1.5 s of deposition (center), to its morphology following 1.2 s of dissolution according to the reciprocal model (right).

which of the atomistic mechanisms discussed in the Model section are likely sources of the orientation dependence of the reaction.

Conclusions

We have presented a new model of electrodeposition and electrodissolution that utilizes Butler-Volmer reaction kinetics, describes facet evolution, tracks the evolution of the electrolyte concentration, and calculates the potential distribution in the electrolyte. The model was implemented using the phase field and smoothed boundary methods, enabling practical 3D simulations of electrodeposition and dissolution with length scales of hundreds of nanometers and time scales of seconds.

Experimental imaging of Mg deposits after short periods of deposition indicates that most of the deposits are broad hexagonal plates with their broad facets either parallel or approximately perpendicular to the substrate. Simulations exhibiting both of these characteristic morphologies were presented.

The morphology of the deposits during growth was demonstrated to depend on the applied current density. At low current densities, the deposits grew in accordance with the kinetic Wulff construction. As the applied current density increases, the deposits become narrower and taller and, at 10 mA/cm^2, develop slanted side facets. Comparisons with simulation results of well-supported and well-stirred electrolytes indicate that this morphological change is due to the depletion of the electrolyte near the side facets, rather than the focusing of the electric field.

Simulations of two deposit spacings, 100 nm and 175 nm, demonstrated a strong dependence of the range of the electrolyte concentration along the electrode surface on both the applied current and the deposit spacing. These findings support Matsui's hypothesis[4] that electrolyte depletion near the deposits inhibits the growth of existing deposits during the early stages of deposition, thereby promoting the nucleation of new deposits.

Two models for the relationship between the orientation dependence of the deposition and dissolution reaction rate constants, the symmetric and reciprocal models, were presented along with likely physical mechanisms underpinning each model. The symmetric model predicts that 45° side facets form during dissolution, leading to a flat-topped hexagonal pyramid morphology. Alternatively, the reciprocal model predicts that the side facets of in-plane hexagonal plates will remain perpendicular to the substrate during dissolution and the deposit retains its hexagonal plate morphology. These simulated morphologies provide testable predictions that can be examined by future experiments.

While we focused on Mg deposition on a noble substrate in this paper, the approach could also be applied to the evolution of bulk Mg anodes. For Mg substrates covered with a thin passive film,[39] deposition would again likely occur through a nucleation process, but potentially with a different crystallographic orientation. Therefore, the details of the deposit morphology may vary depending on the nucleus orientation, and the orientation dependence of the reaction rates could be rotated to simulate these cases. Nevertheless, the general findings of this paper, such as the depletion of electrolyte, would still apply under similar simulated conditions. To describe the extended cycling of bulk Mg anodes, as seen experimentally in Ref. 39, the model may need to be extended to include a treatment of the passivation process.

Improving Mg anode performance is a critical step in the development and commercialization of rechargeable Mg batteries. The features of the model presented here provide the ability to link macroscopic quantities (e.g., the applied current density) to local quantities on the nanometer scale (e.g., the electrolyte concentration at a given point on the electrode surface). Because the evolution of these local quantities determines the electrochemical behavior of the system, improved understanding of the mechanisms governing these phenomena provides new routes for optimizing the performance of Mg batteries.

Acknowledgment

This work was supported as part of the Joint Center for Energy Storage Research, an Energy Innovation Hub funded by the U.S. Department of Energy, Office of Science, Basic Energy Sciences. This research used resources of the National Energy Research Scientific Computing Center, a DOE Office of Science User Facility supported by the Office of Science of the U.S. Department of Energy under Contract No. DE-AC02-05CH11231. S. D. would also like to thank Drs. Hui-Chia Yu and Larry Aagesen for discussions regarding how their previous work could be applied to this research.

References

1. J. Muldoon, C. B. Bucur, A. G. Oliver, T. Sugimoto, M. Matsui, H. S. Kim, G. D. Allred, J. Zajicek, and Y. Kotani, *Energy Environ. Sci.*, **5**, 5941 (2012).
2. H. D. Yoo, I. Shterenberg, Y. Gofer, G. Gershinsky, N. Pour, and D. Aurbach, *Energy Environ. Sci.*, **6**, 2265 (2013).
3. D. Aurbach, Z. Lu, A. Schechter, Y. Gofer, H. Gizbar, R. Turgeman, Y. Cohen, M. Moshkovich, and E. Levi, *Nature*, **407**, 724 (2000).
4. M. Matsui, *J. Power Sources*, **196**, 7048 (2011).
5. J. Tarascon and M. Armand, *Nature*, **414**, 359 (2001).
6. H. Kim, G. Jeong, Y. U. Kim, J. H. Kim, C. M. Park, and H. J. Sohn, *Chem. Soc. Rev.*, **42**, 9011 (2013).
7. F. Mizuno, N. Singh, T. S. Arthur, P. T. Fanson, M. Ramanathan, A. Benmayza, J. Prakash, Y. Liu, P. Glans, and J. Guo, *Front. Energy Res*, **2**, 00046 (2014).
8. S. Yagi, A. Tanaka, T. Ichitsubo, and E. Matsubara, *ECS Electrochem. Lett.*, **1**, D11 (2012).
9. Y. Guo, J. Yang, Y. NuLi, and J. Wang, *Electrochem. Comm.*, **12**, 1671 (2010).
10. D. Aurbach, A. Schechter, M. Moshkovich, and Y. Cohen, *J. Electrochem. Soc.*, **148**A1004 (2001).
11. N. Amir, Y. Vestfrid, O. Chusid, Y. Gofer, and D. Aurbach, *J. Power Sources*, **174**, 1234 (2007).
12. Q. Ju, Y. Shi, and J. Kan, *Synth. Met.*, **178**, 27 (2013).
13. Y. NuLi, J. Yang, and R. Wu, *Electrochem. Comm.*, **7**, 1105 (2005).
14. M. Jäckle and A. Groß, *J. Chem. Phys.*, **141**, 174710 (2014).
15. C. Ling, D. Banerjee, and M. Matsui, *Electrochem. Acta*, **76**, 270 (2012).
16. D. Wheeler, D. Josell, and T. P. Moffat, *J. Electrochem. Soc.*, **150**, C302 (2003).
17. J. Guyer, W. Boettinger, J. Warren, and G. McFadden, *Phys. Rev. E: Stat., Nonlinear, Soft Matter Phys.*, **69**, 021603 (2004).
18. J. Guyer, W. Boettinger, J. Warren, and G. McFadden, *Phys. Rev. E: Stat., Nonlinear, Soft Matter Phys.*, **69**, 021604 (2004).
19. D. R. Ely, A. Jana, and R. E. García, *J. Power Sources*, **272**, 581 (2014).
20. L. K. Aagesen, L. K. Lee, P.-C. Ku, and K. Thornton, *J. Cryst. Growth*, **361**, 57 (2012).
21. L. K. Lee, L. K. Aagesen, K. Thornton, and P.-C. Ku, *Phys. Status Solidi*, **211**, 531 (2014).
22. F. Frank, in *Growth and Perfection of Crystals*, , and R. H. Doremus, B. W. Roberts, and D. Turnbull, Editors, p. 411, Wiley: New York, NY, (1958).
23. H.-C. Yu, H.-Y. Chen, and K. Thornton, *Modell. Simul. Mater. Sci. Eng.*, **20**, 075008 (2012).
24. J. Newman and K. E. Thomas-Alyea, *Electrochemical Systems*, 3rd ed. , John Wiley & Sons: Hoboken, NJ, (2004).
25. B. Orvananos, T. R. Ferguson, H.-C. Yu, M. Z. Bazant, and K. Thornton, *J. Electrochem. Soc.*, **161**, A535 (2014).
26. B. Orvananos, R. Malik, H.-C. Yu, A. Abdellahi, C. P. Grey, G. Ceder, and K. Thornton, *Electrochim. Acta*, **137**, 245 (2014).
27. S. M. Wise, J. S. Lowengrub, J. S. Kim, and W. Johnson, *Superlattices and Microstructures*, **36**, 293 (2004).
28. S. M. Wise, J. S. Lowengrub, J. S. Kim, K. Thornton, P. W. Voorhees, and W. C. Johnson, *Appl. Phys. Lett.*, **87**, 133102 (2005).
29. J. J. Eggleston and P. W. Voorhees, *Appl. Phys. Lett.*, **80**, 306 (2002).
30. Y. Sun and C. Beckermann, *J. Comput. Phys.*, **220**, 626 (2007).
31. J. W. Cahn and J. E. Hilliard, *J. Chem. Phys.*, **28**, 258 (1958).
32. J. Genders and D. Pletcher, *J. Electroanal. Chem.*, **199**, 93 (1986).
33. A. Benmayza, M. Ramanathan, T. S. Arthur, M. Matsui, F. Mizuno, J. Guo, P. Glans, and J. Prakash, *J. Phys. Chem. C*, **117**, 26881 (2013).
34. *CRC Handbook of Chemistry and Physics*, 95th ed., CRC Press: Boca Raton, FL (2014-2015).
35. D. Porter and K. Easterling, *Phase Transformations in Metals and Alloys*, 2nd ed., Chapman and Hall: London, UK (1992).
36. W. H. Press, S. A. Teukolsky, W. T. Vetterling, and B. P. Flannery, *Numerical Recipes: The Art of Scientific Computing*, 3rd ed., Cambridge University Press: Cambridge, UK (2007).
37. O. Mizrahi, N. Amir, E. Pollak, O. Chusid, V. Marks, H. Gottlieb, L. Larush, E. Zinigrad, and D. Aurbach, *J. Electrochem. Soc.*, **155**, A103 (2008).
38. P. Dandekar, Z. B. Kuvadia, and M. F. Doherty, *Annu. Rev. Mater. Res.*, **43**, 359 (2013).
39. D. J. Wetzel, M. A. Malone, R. T. Haasch, Y. Meng, H. Vieker, N. T. Hahn, A. Gölzhäuser, J.-M. Zuo, K. R. Zavadil, A. A. Gewirth, and R. G. Nuzzo, *ACS Appl. Mater. Interfaces*, **7**, 18406-18414 (2015).